

Article

Visible-Light-Driven CO₂ Reduction into Methanol Utilizing Sol-Gel-Prepared CeO₂-Coupled Bi₂O₃ Nanocomposite Heterojunctions

Mohamed Mokhtar Mohamed Mostafa ^{1,*}, Ahmed Shawky ^{2,*}, Sharif Fakhruz Zaman ³, Katabathini Narasimharao ¹, Mohamed Abdel Salam ¹, Abdulmohsen Ali Alshehri ¹, Nezar H. Khdary ⁴, Sulaiman Al-Faifi ¹ and Abhishek Dutta Chowdhury ⁵

¹ Chemistry Department, Faculty of Science, King Abdulaziz University, P.O. Box 80203, Jeddah 21589, Saudi Arabia

² Nanomaterials and Nanotechnology Department, Advanced Materials Institute, Central Metallurgical R&D Institute (CMRDI), P.O. Box 87, Cairo 11421, Egypt

³ Chemical and Materials Engineering Department, King Abdulaziz University, Jeddah 21589, Saudi Arabia

⁴ King Abdulaziz City for Science and Technology, Riyadh 11442, Saudi Arabia

⁵ College of Chemistry and Molecular Sciences, Wuhan University, Wuhan 430072, China

* Correspondence: mmoustafa@kau.edu.sa (M.M.M.M.); phyashawky@gmail.com (A.S.)



Citation: Mostafa, M.M.M.; Shawky, A.; Zaman, S.F.; Narasimharao, K.; Abdel Salam, M.; Alshehri, A.A.; Khdary, N.H.; Al-Faifi, S.; Chowdhury, A.D. Visible-Light-Driven CO₂ Reduction into Methanol Utilizing Sol-Gel-Prepared CeO₂-Coupled Bi₂O₃ Nanocomposite Heterojunctions. *Catalysts* **2022**, *12*, 1479. <https://doi.org/10.3390/catal12111479>

Academic Editors: Vitali A. Grinberg and Alexander D. Modestov

Received: 11 September 2022

Accepted: 16 November 2022

Published: 19 November 2022

Publisher's Note: MDPI stays neutral with regard to jurisdictional claims in published maps and institutional affiliations.



Copyright: © 2022 by the authors. Licensee MDPI, Basel, Switzerland. This article is an open access article distributed under the terms and conditions of the Creative Commons Attribution (CC BY) license (<https://creativecommons.org/licenses/by/4.0/>).

Abstract: Carbon dioxide (CO₂) photoreduction into renewable fuels over semiconductor photocatalysts has emerged as a green and sustainable alternative for energy production. Consequently, tremendous efforts are being performed to develop robust and sustainable photocatalysts. Therefore, visible-light active nanocomposite photocatalysts composed of 5.0–20.0 wt.% bismuth oxide (Bi₂O₃) and cerium oxide (CeO₂) were synthesized by a sol-gel-based process. The prepared nanocomposites were evaluated for the promoted photocatalytic reduction of CO₂ into methanol (CH₃OH). Various characterizations of the obtained photocatalysts exposed an outstanding development of crystalline structure, morphology, and surface texture due to the presence of Bi₂O₃. Moreover, the absorbance of light in the visible regime was improved with enhanced charge separation, as revealed by the exploration of optical response, photoluminescence, and photocurrent measurements. The overall bandgap calculations revealed a reduction to 2.75 eV for 15% Bi₂O₃/CeO₂ compared to 2.93 eV for pure CeO₂. Moreover, the adjusted 2.8 g L⁻¹ dose of 15% Bi₂O₃/CeO₂ selectively produced 1300 μmol g⁻¹ CH₃OH after 9 h of visible light irradiation. This photocatalyst also exhibits bearable reusability five times. The improved progression of 15% Bi₂O₃/CeO₂ is denoted by significant charge separation as well as enhanced mobility. This study suggests the application of metal oxide-based heterojunctions for renewable fuel production under visible light.

Keywords: heterojunction photocatalysts; nanostructures; CO₂ conversion; fuel generation; visible light activity

1. Introduction

With the development of the industrial revolution in the last two centuries, several industries have evolved, such as cement [1], fertilizers [2], and aerosols [3]. In addition, the rapid growth of the population with not enough environmental awareness has led to the release of massive waste materials through several activities [4]. The release of greenhouse gases proportionally increased and contributed to the significant rise in the earth's temperature, with a threat value close to 1.5 °C [5,6]. Thus, reducing, capturing, or recycling greenhouse gases is a matter of life or death for humanity. Carbon dioxide gas (CO₂) is the primary source of global warming that is currently humped due to various human activities ranging from burning fossil fuels to the rapid development of several industries [7,8]. There are several approaches for reducing CO₂ emissions through the use of

renewable energy sources or recycling the released CO₂ into value-added products [9–13]. The photoconversion of CO₂ into valuable and renewable hydrocarbon fuels on semiconductor photocatalysts has caused substantial apprehension toward the clean invention of alternative energy resources [14–17]. The photoreduction of CO₂ either in the gas or liquid phase is an ecological pathway owing to its simplicity and sustainability, particularly regarding conservational topics [18,19]. The catalytic conversion of CO₂ into value-added products, such as methanol (CH₃OH) or other organic materials, is an additional benefit to the global warming issue [17,20,21]. As a consequence, plentiful research is currently being performed to advance this approach by utilizing simulated and natural solar light [22–24]. In the meantime, abundant ceramic-based photocatalysts demonstrate effectual progress in several fields, such as pollutant degradation and fuel production [25–29]. Notably, TiO₂ and ZnO represent famous oxides for fuel production and the photocatalytic reduction of CO₂ owing to their suitable reduction potential balanced within their bandgap energies (E_g) [30–33]. However, the extended E_g, photostability in solutions, and the rapid recombination of the photoinduced charges are key issues in the realization of these oxides [34,35]. Therefore, there are several efforts regarding the coupling of these oxides with more stable ceramics to enhance their stability [31,36–38]. The use of other stable ceramic oxides with comparable E_g represents an alternative path [39,40].

Interestingly, the use of rare-earth metal oxides such as cerium oxide (CeO₂) is promising in photocatalysis. In a recent study by Hezam et al., the nanostructured CeO₂ with controlled oxygen vacancies could be efficient for the photoreduction of CO₂ into CH₃OH [41]. Moreover, CeO₂ has narrower E_g (2.8–3.1 eV) than TiO₂ and ZnO, exhibiting an n-type character and representing a more stable ceramic oxide with potential applications in various photocatalytic reactions, including water splitting [42], organic transformation reactions [43], and pollutant degradation [44]. Moreover, the coupling with p-type oxides such as bismuth oxides (Bi₂O₃) showed a significant photocatalytic performance in dye degradation [37,45], self-cleaning coatings [46], and NO oxidation [47]. In a recent study performed by Yang et al., the β-Bi₂O₃-loaded CeO₂ heterostructure photocatalyst exhibited a significant redox for the oxidation of stable antibiotic molecules due to the enhanced charge separation of the added β-Bi₂O₃ in the heterojunction system [48]. Moreover, Masula et al. investigated the improved photocatalytic performance of Bi₂O₃/CeO₂ nanocomposites for the mineralization of wastewater pollutants in a short time due to their enhanced visible-light absorbance [49]. However, there are no studies regarding the photoreduction of CO₂ as far as we know. It could be of great scientific and industrial benefit regarding the ability of this nanocomposite in the renewable reforming of CO₂ into valuable and usable fuels. In this regard, nanostructured CeO₂ was simply prepared using the polymeric surfactant-assisted sol-gel method and subsequently coupled with 5.0–20.0 wt.% of Bi₂O₃. The prepared Bi₂O₃/CeO₂ heterojunctions featured a mesoporous surface texture, amended light harvesting, and superior photogenerated charge separations as concluded from the detailed characterization. The photoreduction of CO₂ into selective CH₃OH production over the optimized 15% Bi₂O₃/CeO₂ presented a generation rate of 144.4 μmol g^{−1} h^{−1} and demonstrated robust stability for regeneration.

2. Results and Discussion

2.1. Structural, Surface, and Optical Investigations of the Produced Photocatalysts

The formed materials were identified by XRD graphs as described in Figure 1 for the pure sample in **a** compared to the Bi³⁺-added samples in **b**, **c**, **d**, and **e** for 5, 10, 15, and 20 wt.%. The pure sample **a** was identically identified as pure CeO₂ by the coincident 2θ values of 28.5°, 32.8°, 47.5°, 56.0°, and 59.1° to the (1 1 1), (2 0 0), (2 2 0), (3 1 1), and (2 2 2) planes of cubic CeO₂ as described in JCPDS card No. 34–0394, respectively [50]. Similarly, the 5% Bi³⁺ precursor addition (represented by **b**) did not alter the overall pattern due to the limited detection of minor contamination of the XRD instrument. However, the further addition of the Bi³⁺ precursor in **c–e** resulted in the appearance of new diffraction peaks, mainly existing at 27.6°, 35.2°, 39.1°, 45.1°, and 45.4° assigned to (201), (200), (321),

(222), and (421) of the β -phase of Bi_2O_3 (JCPDS No. 76–0147) [20]. Thus, the $\text{Bi}_2\text{O}_3/\text{CeO}_2$ nanocomposite formation was revealed by XRD depiction [51].

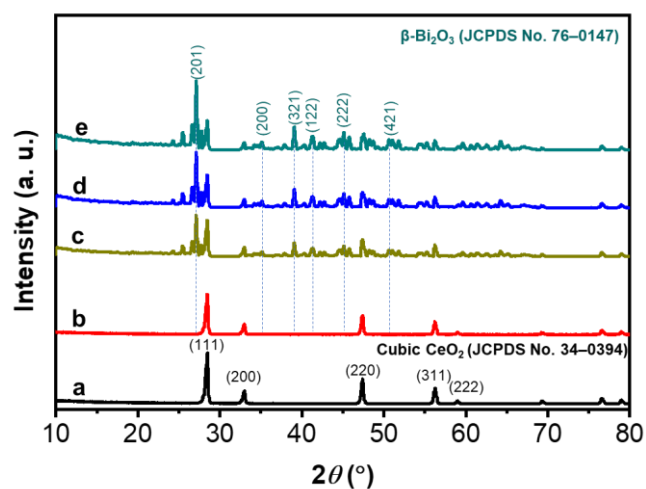


Figure 1. XRD patterns of the produced powders representing the crystallization of pure CeO_2 (as labeled in a compared with 5, 10, 15, and 20% $\text{Bi}_2\text{O}_3/\text{CeO}_2$ as represented by b, c, d, and e, respectively).

TEM images describing the morphology of the pure CeO_2 compared with various Bi_2O_3 -added CeO_2 nanostructures can be seen in Figure 2. The pure CeO_2 indicated the formation of irregular-shaped nanocrystals with well-defined edges (Figure 2a). The particle size of the CeO_2 nanocrystals ranged between 20 and 40 nm. The magnified elected area at a high resolution (Figure 2b) confirmed the face-centered cubic phase of CeO_2 owing to the d-spacing measurement of 0.31 nm representing the (111) plane [46]. The Bi_2O_3 -loading of CeO_2 revealed certain changes to the structure and morphology as seen in Figure 2c–h. In Figure 2c, representing 5% $\text{Bi}_2\text{O}_3/\text{CeO}_2$, small spherical nanoparticles were seen side-by-side with the CeO_2 nanocrystals of <10 nm as represented by black–white arrows [51]. The high-resolution TEM image of the selected part of this revealed the formation of Bi_2O_3 nanocrystals due to the measured d-spacing (0.2 nm) of the (222) plane as shown in Figure 2d [48]. On the other hand, the higher content of Bi_2O_3 at 10 wt.% (Figure 2e) and 15 wt.% (Figure 2g) showed an elongation of its Bi_2O_3 structure assigned by the representative black–white arrows. The Bi_2O_3 was grown in a rod-like morphology but maintained the same crystalline phase as confirmed by the d-spacing measurements in the high-resolution images (Figure 2f,h) without any effect on the CeO_2 nanocrystals. This refers to the fact that the solution-based β - Bi_2O_3 is usually grown in a rod-like structure [20,40,49]. These findings indicate the successful fabrication of the $\text{Bi}_2\text{O}_3/\text{CeO}_2$ heterojunction. The close contact between the Bi_2O_3 and CeO_2 could enhance the charge transfer amongst them and explain the efficient photocatalytic activity toward the production of CH_3OH [48,49,51].

To clarify the surface texture of the obtained $\text{Bi}_2\text{O}_3/\text{CeO}_2$ heterojunctions, the N_2 adsorption–desorption isotherms comparing pure CeO_2 and 15% $\text{Bi}_2\text{O}_3/\text{CeO}_2$ photocatalysts are shown in Figure 3. Both samples exhibited minor adsorption at a relative pressure (P/P_0) of 0.65 and an H_2 -hysteresis loop with type IV until $P/P_0 = 0.94$ [45]. This finding designates that the prepared samples parade a mesoporous structure. The inclusion of Bi_2O_3 has no significant effect on the superficial structure but slightly changes the S_{BET} and pore diameters (inset of Figure 3). The determined S_{BET} is comparatively decreased by including Bi_2O_3 to CeO_2 from 191 to 169 $\text{m}^2 \text{g}^{-1}$ (for 15% $\text{Bi}_2\text{O}_3/\text{CeO}_2$, Table 1) owing to the spread of smaller-sized Bi_2O_3 on the surface of CeO_2 . However, the pore size is almost the same (8.92 nm for CeO_2 and 8.87 nm for 15% $\text{Bi}_2\text{O}_3/\text{CeO}_2$) as seen in the inset of Figure 3.

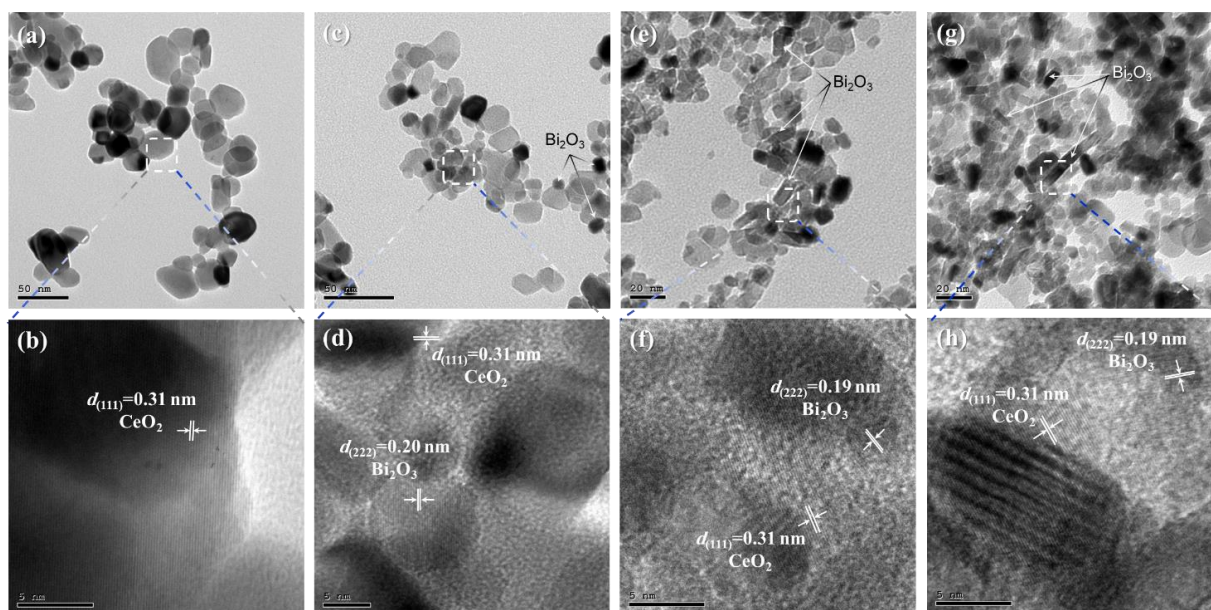


Figure 2. TEM investigations (up) and the corresponding high-resolution imaging for the selected area (down) of pure CeO_2 (a,b), 5% $\text{Bi}_2\text{O}_3/\text{CeO}_2$ (c,d), 10% $\text{Bi}_2\text{O}_3/\text{CeO}_2$ (e,f), and 15% $\text{Bi}_2\text{O}_3/\text{CeO}_2$ (g,h).

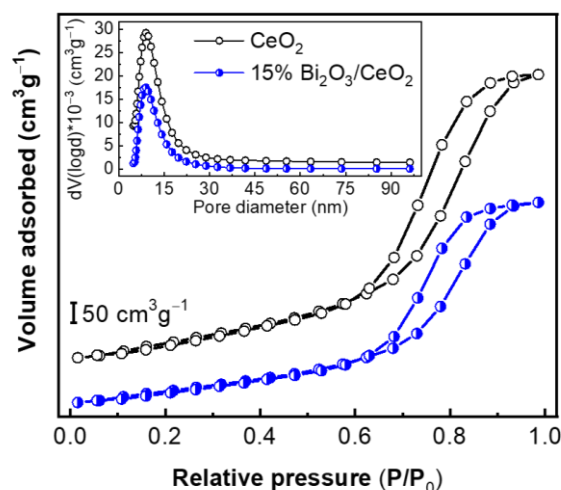


Figure 3. N_2 adsorption/desorption isotherms and corresponding pore size distribution (inset) for prepared CeO_2 compared to 15% $\text{Bi}_2\text{O}_3/\text{CeO}_2$ heterojunctions as indicated.

Table 1. Consequence of Bi_2O_3 inclusion on physicochemical characteristics of CeO_2 , namely, surface area (S_{BET}), absorption edge (Abs. edge), and determined bandgap energies (E_g). The consistent photoreduction of CO_2 to CH_3OH after 9 h irradiation is listed. The corresponding photocurrent intensities are also stated in the last column.

Sample	S_{BET} ($\text{m}^2 \text{g}^{-1}$)	Abs. Edge (nm)	E_g (eV)	CH_3OH Generation ($\mu\text{m g}^{-1}$)	Photocurrent ($\mu\text{A cm}^{-2}$)
CeO_2	191	423	2.93	70 (± 2.8)	11.56
5% $\text{Bi}_2\text{O}_3/\text{CeO}_2$	183	427	2.89	360 (± 12.6)	28.92
10% $\text{Bi}_2\text{O}_3/\text{CeO}_2$	174	442	2.82	720 (± 21.6)	43.52
15% $\text{Bi}_2\text{O}_3/\text{CeO}_2$	169	453	2.75	1080 (± 24.5)	51.54
20% $\text{Bi}_2\text{O}_3/\text{CeO}_2$	163	454	2.74	1100 (± 38.4)	51.81

The surface composition of the 15% $\text{Bi}_2\text{O}_3/\text{CeO}_2$ sample was analyzed via XPS as seen in Figure 4. The Bi 4f the high-resolution spectrum (Figure 4a) was deconvoluted into two

oxidation states for the majority of Bi^{3+} at binding energies of 164.2 and 159.2 eV for $4f_{5/2}$ and $4f_{7/2}$, respectively, and a minority of Bi^{5+} at 165.0 and 160.5 eV for the corresponding mentioned orbitals [49]. The Ce 3d spectrum (Figure 4b) was deconvoluted into the co-existing minority Ce^{3+} and the majority of Ce^{4+} [44]. The Ce^{3+} is located at 902.1 and 886.5 for $3d_{3/2}$ and $3d_{5/2}$ orbitals [46]. On the other hand, the major peaks located at 917.2, 908.2, and 898.7 eV are attributed to the $3d_{3/2}$ binding of Ce^{4+} while the binding energies positioned at 890.2 and 883.1 eV correspond to the $3d_{5/2}$ of Ce^{4+} in CeO_2 . In Figure 4c, the O1s spectrum is deconvoluted into three peaks at 532.4, 530.1, and 529.0 eV assigned to the adsorbed oxygen species, the lattice bonding Bi–O of $\beta\text{-Bi}_2\text{O}_3$, and the lattice bonding Ce–O in CeO_2 , respectively [47]. Thus, the confirmation of the formed $\text{Bi}_2\text{O}_3/\text{CeO}_2$ heterojunction is established by the XPS study. The quantitative analysis using the instrumental software showed the content of Bi_2O_3 in this sample at 13.9 wt.%.

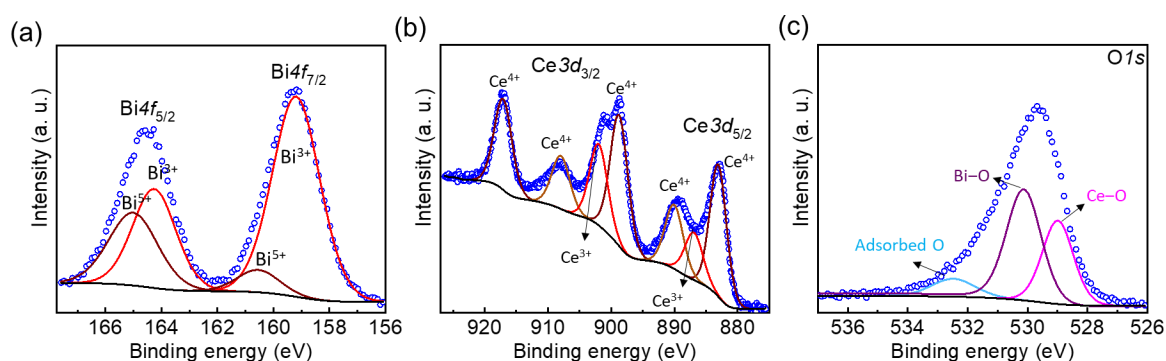


Figure 4. XPS analysis at high resolution for Bi 4f (a), Ce 3d (b), and O 1s (c) of the 15% $\text{Bi}_2\text{O}_3/\text{CeO}_2$ heterojunction.

The light harvesting by the synthesized photocatalysts was also investigated as displayed in Figure 5. The pristine CeO_2 disclosed a minor visible-light absorbance with an absorption edge at 423 nm and an estimated E_g of 2.93 eV [43]. However, the synthesized $\text{Bi}_2\text{O}_3/\text{CeO}_2$ showed an extension of the visible-light harvesting as the absorption edges shifted toward longer wavelengths due to the low-bandgap Bi_2O_3 [48]. The presence of 5, 10, 15, and 20 wt.% Bi_2O_3 in CeO_2 redshifted the absorption edges to 427, 442, 453, and 454 nm, with corresponding E_g values of 2.89, 2.82, 2.75, and 2.74 eV, respectively (Table 1, inset of Figure 5). Thus, the presence of Bi_2O_3 could enhance light harvesting and associated photocatalytic performance [37,49].

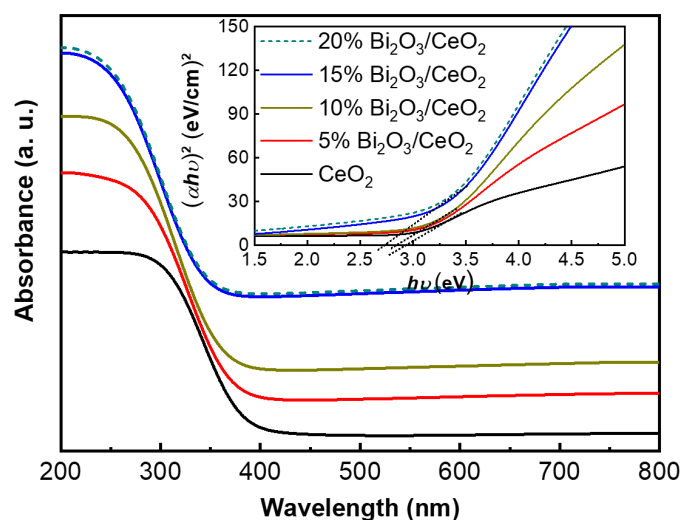


Figure 5. Light absorption spectra of the prepared CeO_2 compared with $\text{Bi}_2\text{O}_3/\text{CeO}_2$ heterojunctions and their corresponding calculated energy gaps as seen in the inset.

2.2. Photoreduction of CO₂ over Bi₂O₃/CeO₂ Heterojunctions

The photocatalytic progression of the produced Bi₂O₃/CeO₂ is evaluated for the reduction of CO₂ as described in Figure 6 compared to the pure CeO₂. In Figure 6a, the photocatalytic generation of CH₃OH of Bi₂O₃/CeO₂ is much higher than the pure CeO₂ after 9 h of light irradiation as seen in Table 1. The production rate of CH₃OH reached 120.0 and 122.2 μmol g⁻¹ h⁻¹ by 15 and 20% Bi₂O₃/CeO₂, respectively, which is almost 15.4 and 15.7 times higher than the pure CeO₂ at the same 2.0 g L⁻¹ dose (7.8 μmol g⁻¹ h⁻¹, Figure 6b). As a result, the photoreduction of CO₂ into CH₃OH can be surged by governing the amount of Bi₂O₃. The 15 wt.% of Bi₂O₃ is chosen as the optimal included amount in the Bi₂O₃/CeO₂ heterojunction based on the above results.

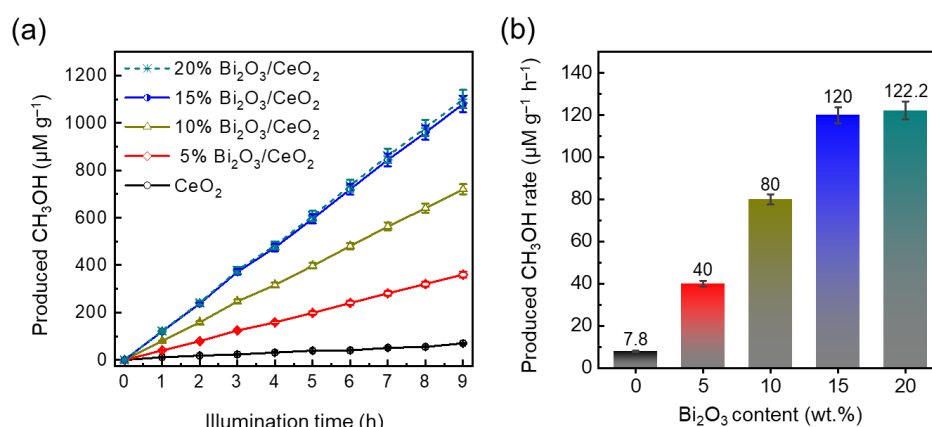


Figure 6. Photocatalytic production of CH₃OH utilizing the produced CeO₂ and Bi₂O₃/CeO₂ heterojunctions as in (a). The influence of adding Bi₂O₃ on the generation rate of produced CH₃OH is illustrated in (b).

Photoluminescence (PL) spectral emission and photocurrent intensity are regarded as powerful means for understanding the photocatalytic activity promotion of the 15% Bi₂O₃/CeO₂ as seen in Figure 7 [41,52,53]. In Figure 7a, we can see that the pure CeO₂ exhibited an intensive PL peak positioned at 406.3 nm due to the large recombination of the photogenerated charges [44]. The introduction of 5, 10, 15, and 20 wt.% Bi₂O₃ amounts clearly quenched the PL intensity by 12, 21, 32, and 32.1%, respectively. These results indicate the suppression of the charge carrier's recombination rates. So, the catalytic activity could be increased by the long-life charge carriers as proved in previous PL quenching due to the precise Bi₂O₃ occurrence in the 15% Bi₂O₃/CeO₂ heterojunction. Moreover, transient photocurrent measurements have also established the best photocatalytic performance of the same 15% Bi₂O₃/CeO₂ nanocomposite as presented in Figure 7b and Table 1. The 15% Bi₂O₃/CeO₂ exhibited the largest photocurrent value (51.54 μA cm⁻²), which is almost 4.5 times higher than the photocurrent generated from pure CeO₂. This finding reveals the promoted charge mobility due to the superior separation of the photoinduced charge carriers. Accordingly, the photoreduction rate of CO₂ could be enhanced using this optimal photocatalyst.

The dose tuning plays a key role in the photoactivity of nanocomposite photocatalysts due to the upsurging of photoactive sites that are balanced with the adsorbed target molecules and light photons [54–58]. Figure 8a displays the impact of dose alteration (0.7–3.5 g L⁻¹) of 15% Bi₂O₃/CeO₂ on the photocatalytic generation of CH₃OH. The dose-dependent generation of CH₃OH parades the comparative upsurge from 608 (±19.5) to a maximum of 1300 (±41.6) μM g⁻¹ for 0.7 and 2.8 g L⁻¹, correspondingly, after 9 h of visible-light illumination. This outcome exhibits the improvement of the photocatalytic active spots bared to CO₂ molecules in the case of 2.8 g L⁻¹ compared to other doses. Nevertheless, the extra dose of the 15% Bi₂O₃/CeO₂ at 3.5 g L⁻¹ decreased the CH₃OH generation to 1230 (±39.4) μmol g⁻¹. Accordingly, the dosage accumulation could moderately impede the light photons from reaching the photocatalyst's surface, resulting in a reduction of the

overall activity [59,60]. Thus, 2.8 g L^{-1} is the optimized dose for the 15% $\text{Bi}_2\text{O}_3/\text{CeO}_2$ that exhibits the highest generation rate of CH_3OH as described in Figure 8b and proven by chromatograms in Figure S2 (supplementary materials). The spent 15% $\text{Bi}_2\text{O}_3/\text{CeO}_2$ photocatalyst was also tested for recyclability as presented in Figure 8c. The outcomes showed that the optimal 15% $\text{Bi}_2\text{O}_3/\text{CeO}_2$ validates five-time reusability for the CO_2 reduction under visible light to CH_3OH at $1274 \mu\text{mol g}^{-1}$, which is 98% of its initial value in the first run. The XRD and TEM investigations for the spent material did not show any significant structural changes (Figure S3, supplemental data). Therefore, the 15% $\text{Bi}_2\text{O}_3/\text{CeO}_2$ exhibits a workable photocatalytic application for CO_2 reduction beneath visible light.

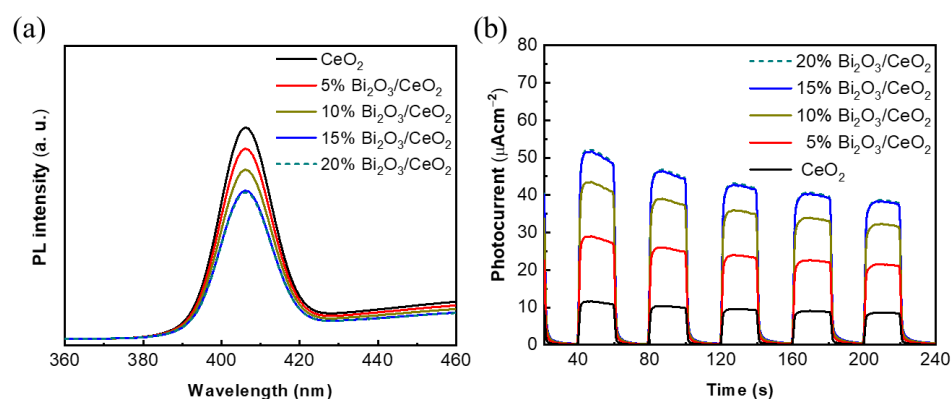


Figure 7. PL spectra (a) and transient photocurrents (b) of pure CeO_2 and $\text{Bi}_2\text{O}_3/\text{CeO}_2$ heterojunctions as stated.

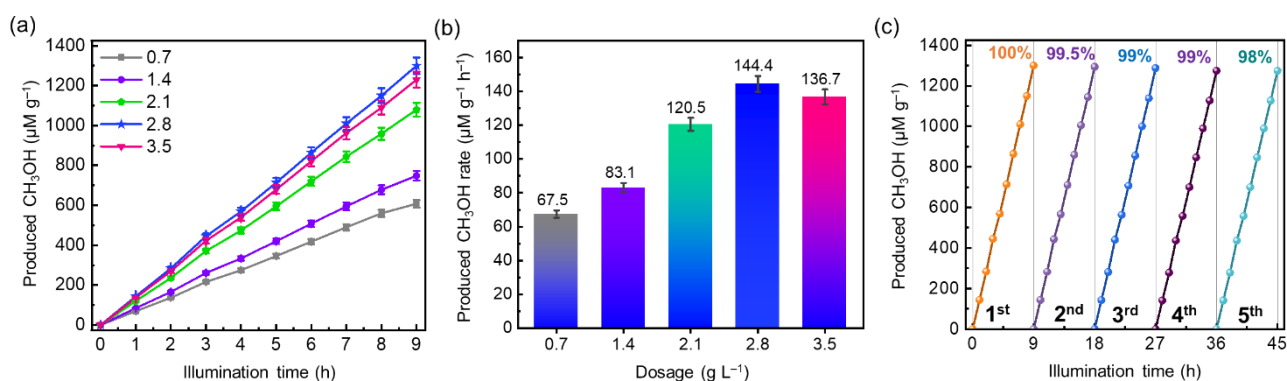


Figure 8. Photocatalytic production of CH_3OH over different doses (in g L^{-1}) of 15% $\text{Bi}_2\text{O}_3/\text{CeO}_2$ heterojunctions as in (a). The influence of dosage on the generation rate of produced CH_3OH is illustrated in (b). The reusability of the best-performing spent photocatalyst dose (2.8 g L^{-1}) is illustrated in (c).

Finally, the photoreduction pathway could be proposed as seen in Figure 9 based on previous discussions. The represented band diagrams of p-type Bi_2O_3 and n-type CeO_2 can be calculated by the following formula (supplementary materials S-4):

$$E_{\text{CB}} = \chi - E_e - 0.5E_g \quad (1)$$

$$E_{\text{VB}} = E_{\text{CB}} + E_g \quad (2)$$

where E_{VB} and E_{CB} are the valence (VB) and conduction (CB) band potentials versus the standard hydrogen electrode (NHE), respectively. E_e is the energy of free electrons and χ is the electronegativity of the semiconductor photocatalyst, which is determined in supplementary materials [61–63]. Thus, upon illumination of both semiconductors by visible light, the photoinduced charge carriers, namely electrons (e^- s), are generated at

−0.405 and +0.535 eV corresponding to the CB of Bi₂O₃ and CeO₂, respectively, while the holes (*h*⁺s) were located at +2.525 and +2.93, corresponding to VB of Bi₂O₃ and CeO₂, respectively. Since the p-n heterojunction is formed between p-type Bi₂O₃ and n-type CeO₂, an electric field (signed as *E*) is designed at the interface of the formed heterojunction and band-bending occurs due to the unified Fermi levels [64–66]. Thus, the excited *e*[−]s at the CB of p-type Bi₂O₃ could recombine with the *h*⁺s left at the VB of n-type CeO₂ by the driving electric field effect [67]. On the other hand, the high redox potential *e*[−]s on the CB of CeO₂ and *h*⁺s on the VB of Bi₂O₃ can contribute to the photoreduction of CO₂ as follows: The H₂ molecules could react with the *h*⁺s resulting in the splitting reaction to protons, oxygen, and free *e*[−]s as shown in Equation (3) [68,69].

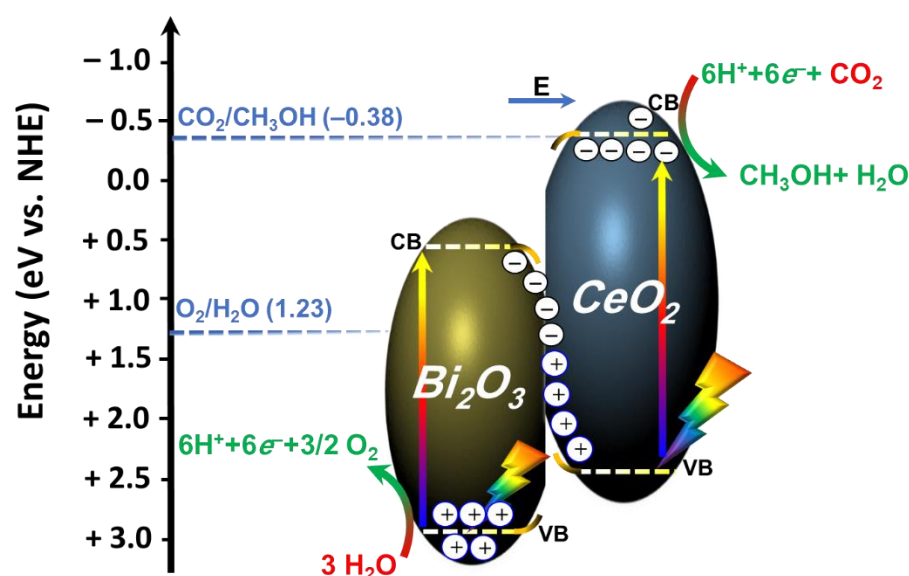
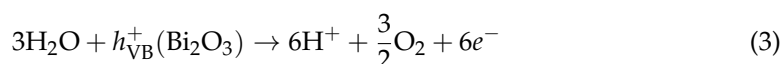
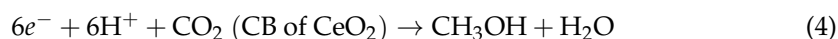


Figure 9. Estimated band diagrams, charge transfer, and photocatalytic pathway for CO₂ conversion into methanol over optimized Bi₂O₃/CeO₂ heterojunctions.

At last, at the CB of CeO₂, which is very close to the reduction potential of CO₂ into CH₃OH [68,70], the produced protons and *e*[−]s in (3) can selectively convert the CO₂ to CH₃OH as in (4)



Therefore, the improved, recyclable, and efficient 15% Bi₂O₃/CeO₂ heterojunctions reveal the promoted photoconversion of CO₂ to an alternative renewable fuel under visible-light illumination.

3. Experiments

3.1. Chemicals

All materials were purchased from Merck in this work without subsequent treatment. The Ce and Bi precursors were Ce(NO₃)₃·6H₂O (99.999% trace metals basis) and Bi(NO₃)₃·5H₂O (99.999% trace metals basis). The polymeric non-ionic surfactant, namely Poly(ethylene glycol)-block-poly(propylene glycol)-block-poly(ethylene glycol) (Pluronic F-108, MW~14,600), was utilized as the growth-limiting reagent and micelle template [71]. Acetic (CH₃COOH, ≥99.7%) and hydrochloric (HCl, ACS reagent, 37%) acids were used in the sol-gel process for hydrolysis and esterification procedures. Ethanol absolute (CH₃CH₂OH, ≥99.8%) and deionized water (DI-H₂O, >18.2 MΩ) were also used for hy-

drollysis and washing purposes. Sodium carbonate (Na_2CO_3 , $\geq 99.5\%$, ACS reagent) was used as the CO_2 source in the photoreaction system.

3.2. Synthesis of CeO_2 and $\text{Bi}_2\text{O}_3/\text{CeO}_2$ Photocatalysts

Nanocrystalline CeO_2 particles were synthesized by a modified sol-gel method in the presence of Pluronic F-108. In detail, 2.0 g of F-108 was disseminated in 40 mL of $\text{CH}_3\text{CH}_2\text{OH}$ under vigorous stirring. After that, 12 mmol of HCl and 40 mmol CH_3COOH were progressively poured under the same conditions and then left for 1 h. Then, 1.63 g of $\text{Ce}(\text{NO}_3)_3 \cdot 6\text{H}_2\text{O}$ was included in the above viscous solution and kept for another 2 h. The cloudy suspended mixture was then transferred into a clean Petri dish for 12 h of polymerization in a humidity chamber operated at 40°C before drying at 65°C for another 24 h. The obtained hard gel was crystallized for 5 h at 650°C to obtain mesostructured CeO_2 nanoparticles. The $\text{Bi}_2\text{O}_3/\text{CeO}_2$ heterojunctions were prepared by impregnating the Bi_2O_3 into the CeO_2 matrix. In brief, 1.0 g of synthesized CeO_2 was sonicated in 100 mL of $\text{CH}_3\text{CH}_2\text{OH}$ for 10 min. Next, 52 mg of $\text{Bi}(\text{NO}_3)_3 \cdot 5\text{H}_2\text{O}$ was familiarized into the solution while stirring and maintained for 1 h. Then, $\text{CH}_3\text{CH}_2\text{OH}$ was evaporated by increasing the temperature to 80°C . After approximately 5 h, the calcination of the dried powder was performed at 600°C for 3 h to crystallize the 5% $\text{Bi}_2\text{O}_3/\text{CeO}_2$ heterojunction. The above procedure was repeated by increasing the Bi^{3+} precursor amount to 104, 156, and 208 mg to obtain 10, 15, and 20% $\text{Bi}_2\text{O}_3/\text{CeO}_2$ nanocomposites.

3.3. Depictive Characterization of the Obtained CeO_2 and $\text{Bi}_2\text{O}_3/\text{CeO}_2$

Numerous instruments have been employed to characterize the produced sample. The Bruker AXS D8 X-ray diffraction (XRD, Billerica, MA, USA) unit explored the crystalline phases of the ground powders. The surface composition of the 15% $\text{Bi}_2\text{O}_3/\text{CeO}_2$ was investigated by the Thermo VG Multilab 2000 X-ray photoelectron spectrometer (XPS, East Grinstead, UK). Regarding the morphology study, a high-resolving-power JEOL-JEM-1230 transmission electron microscope (TEM, Tokyo, Japan) examined the samples dispersed on carbon-coated grids. The Nova Quantachrome analyzer generated N_2 adsorption-desorption (Ostfildern-Scharnhausen, Germany) isotherms to describe the surface texture of the degassed samples at 150°C . The specific surface area (S_{BET}) was calculated based on the Brunauer-Emmett-Teller (BET) formula, which estimates the specific surface area of the prepared structures. The light harvesting of CeO_2 and $\text{Bi}_2\text{O}_3/\text{CeO}_2$ was studied via a Jasco spectrophotometer (V-570, Tokyo, Japan) in the 200–800 nm spectral range. The bandgap energy (E_g) was determined based on the modified Tauc formula through their diffusive reflectance. Photoluminescence emission (PL) was investigated by an RF-5301 fluorescence spectrometer (Shimadzu, Kyoto, Tapan) in ambience. Lastly, the electrochemical workstation (Zahner Zennium, Ostfildern-Scharnhausen, Germany) measured the transient photocurrents of the $0.3 \times 0.3 \text{ cm}^2$ working electrodes composed of each sample on Ti foil at zero bias during the ON and OFF states of 1.0 mW cm^{-2} light illumination.

3.4. Setup for Photoreduction of CO_2

The photoreduction experiments were performed in a homemade photoreactor containing a 250 mL two-neck quartz flask. The simulated visible light was provided by a 300 W Xe lamp (Newport, CA, USA, 45.2 mW cm^{-2}) equipped with a 420 nm cut-off filter. In detail, a certain dose of the synthesized photocatalyst was dispersed in 125 mL of H_2O before being heated to 80°C . Then, 135 mg of Na_2CO_3 was inserted into the above suspension. Moreover, nitrogen gas was initially introduced for 30 min to ensure an inert atmosphere at 100 sccm. After that, 0.315 mL of 4 M HCl was gently injected to generate CO_2 . The whole system was kept in murky conditions for 1 h to settle the equilibrium. The photoreactor was then irradiated by visible light. At fixed one-hour intervals, a gas chromatograph (GC-FID, Shimadzu) equipped with a flame ionization detector was employed to sense the formed products through the photoreaction [68]. The produced spectra generated by the detection unit were compared with the standard GC spectra of 2.5 mM L^{-1} CH_3OH

solution (supplementary Figure S1) [21]. The produced CH₃OH was recognized in the above-mentioned spectra under the same experimental conditions using the GC. Generally, neither CH₃OH nor other products are detected before light illumination. The reusability of the spent photocatalyst for five independent cycles was performed via simple drying under ambient conditions for 1 h at 120 °C.

4. Conclusions

A facile sol-gel-based method was applied for the fabrication of the Bi₂O₃/CeO₂ heterojunction photocatalyst. The precise addition of p-type Bi₂O₃ amended the absorbance in the visible light regime through the reduction of the overall bandgap of the produced Bi₂O₃/CeO₂ heterojunction down to 2.74 eV. The various Bi₂O₃-included CeO₂ were applied for the selective photocatalytic reduction of CO₂ into methanol beneath visible light. The 2.8 g L⁻¹ dose of 15% Bi₂O₃/CeO₂ generated 1300 μmol/g of CH₃OH within 9 h of illumination, nearly 18.6-fold higher than pure CeO₂. This optimized heterojunction verified the five-time reusability at 98% of its initial performance. The substantial photoactivity of Bi₂O₃/CeO₂ is attributed to the significant photogenerated charge separation in addition to the amended harvesting of light. This work provides plenty of room for the future of renewable fuel production from CO₂ utilizing metal oxide-based heterostructure photocatalysts.

Supplementary Materials: The following supporting information can be downloaded at: <https://www.mdpi.com/article/10.3390/catal12111479/s1>, Figure S1: Gas chromatograph of standard 2.5 mM/L CH₃OH solution showing a single peak at 2.46 min retention. The spectra is used as a reference to compare the selective photoreduction of CO₂ over the prepared Bi₂O₃/CeO₂ nanocomposites in the main manuscript; Figure S2: Gas chromatograph of the produced product over the optimized dose 2.8 g/L of 15% Bi₂O₃/CeO₂ showing the accumulated production of CH₃OH over time of irradiation; Figure S3: XRD patterns (a) and TEM images (b) of the spent nanocomposite after the first and the fifth runs displaying no substantial change in the crystalline phase or morphological structure after recycling for five times.

Author Contributions: Conceptualization, M.M.M.M., A.S and A.D.C.; methodology, M.A.S. and A.A.A.; software, M.M.M.M., A.S., S.F.Z. and S.A.-F.; validation, N.H.K.; formal analysis, S.F.Z., A.S. and K.N.; investigation, A.S., K.N. and A.A.A.; resources, S.A.-F.; data curation, A.S., M.A.S. and A.D.C.; writing—original draft, A.S. and A.D.C.; writing—review and editing, M.M.M.M. and A.S.; visualization, N.H.K.; supervision, A.S.; project administration, M.M.M.M.; funding acquisition, M.M.M.M. All authors have read and agreed to the published version of the manuscript.

Funding: This research was funded by Deanship of Scientific Research (DSR), King Abdulaziz University, Jeddah, Saudi Arabia (NO. IFPRC-108-130-2020).

Data Availability Statement: Data is contained within the article or supplementary material.

Acknowledgments: The authors extend their appreciation to the Deputyship for Research & Innovation, Ministry of Education in Saudi Arabia for funding this research work through project number IFPRC-108-130-2020 and the Deanship of Scientific Research (DSR), King Abdulaziz University, Jeddah, Saudi Arabia.

Conflicts of Interest: The authors declare no conflict of interest.

References

1. Plaza, M.G.; Mart, S.; Rubiera, F. CO₂ Capture, Use, and Storage in the Cement Industry: State of the Art and Expectations. *Energies* **2020**, *13*, 5692. [CrossRef]
2. Kang, S.M.; Adhikari, A.; Bhatta, D.; Gam, H.J.; Gim, M.J.; Son, J.I.; Shin, J.Y.; Lee, I.J. Comparison of Effects of Chemical and Food Waste-Derived Fertilizers on the Growth and Nutrient Content of Lettuce (*Lactuca Sativa* L.). *Resources* **2022**, *11*, 21. [CrossRef]
3. Gao, Y.; Zhuang, B.; Wang, T.; Chen, H.; Li, S.; Wei, W.; Lin, H.; Li, M. Climatic–Environmental Effects of Aerosols and Their Sensitivity to Aerosol Mixing States in East Asia in Winter. *Remote Sens.* **2022**, *14*, 3539. [CrossRef]
4. Modarress Fathi, B.; Ansari, A.; Ansari, A. Threats of Internet-of-Thing on Environmental Sustainability by E-Waste. *Sustainability* **2022**, *14*, 161. [CrossRef]
5. Valipour, M.; Bateni, S.M.; Jun, C. Global Surface Temperature: A New Insight. *Climate* **2021**, *9*, 81. [CrossRef]

6. Siddique, R.; Mejia, A.; Mizukami, N.; Palmer, R.N. Impacts of Globalwarming of 1.5, 2.0 and 3.0 °C on Hydrologic Regimes in the Northeastern U.S. *Climate* **2021**, *9*, 9. [[CrossRef](#)]
7. Ata, B.; Pakrooh, P.; Barkat, A.; Benhizia, R.; Pénczes, J. Inequalities in Regional Level Domestic CO₂ Emissions and Energy Use: A Case Study of Iran. *Energies* **2022**, *15*, 3902. [[CrossRef](#)]
8. Zhang, C.; Zhang, W.; Luo, W.; Gao, X.; Zhang, B. Analysis of Influencing Factors of Carbon Emissions in China's Logistics Industry: A Gdim-Based Indicator Decomposition. *Energies* **2021**, *14*, 5742. [[CrossRef](#)]
9. Pires, L.; Vaz, M.; Carolina, A.; De Oliveira, C.; Falcon, L.; Stella, M.; Pimenta, S.; Bessa, I.G.; Wouters, J.; Andrade, H.S.; et al. Capture and Reuse of Carbon Dioxide (CO₂) for a Plastics Circular Economy: A Review. *Processes* **2021**, *9*, 759. [[CrossRef](#)]
10. Catizzone, E.; Bonura, G.; Migliori, M.; Frusteri, F.; Giordano, G. CO₂ Recycling to Dimethyl Ether: State-of-the-Art and Perspectives. *Molecules* **2018**, *23*, 31. [[CrossRef](#)]
11. Nebel, A.; Cantor, J.; Salim, S.; Salih, A.; Patel, D. The Role of Renewable Energies, Storage and Sector-Coupling Technologies in the German Energy Sector under Different CO₂ Emission Restrictions. *Sustainability* **2022**, *14*, 10379. [[CrossRef](#)]
12. Sarkar, M.; Chung, B. Do Effect of Renewable Energy to Reduce Carbon Emissions under a Flexible Production System: A Step toward Sustainability. *Energies* **2021**, *14*, 215. [[CrossRef](#)]
13. Materials, M. Supercritical CO₂ Curing of Resource-Recycling Secondary Main Materials. *Materials* **2022**, *15*, 4581.
14. Hussain, S.; Wang, Y.; Guo, L.; He, T. Theoretical Insights into the Mechanism of Photocatalytic Reduction of CO₂ over Semiconductor Catalysts. *J. Photochem. Photobiol. C Photochem. Rev.* **2022**, *52*, 100538. [[CrossRef](#)]
15. Jerome, M.P.; Alahmad, F.A.; Salem, M.T.; Tahir, M. Layered Double Hydroxide (LDH) Nanomaterials with Engineering Aspects for Photocatalytic CO₂ conversion to Energy Efficient Fuels: Fundamentals, Recent Advances, and Challenges. *J. Environ. Chem. Eng.* **2022**, *10*, 108151. [[CrossRef](#)]
16. Sundar, D.; Karuppasamy, L.; Gurusamy, L.; Liu, C.H.; Wu, J.J. Perovskites-like Composites for CO₂ Photoreduction into Hydrocarbon Fuels. *Curr. Opin. Green Sustain. Chem.* **2022**, *33*, 100563. [[CrossRef](#)]
17. Kumar, A.; Singh, P.; Khan, A.A.P.; Van Le, Q.; Nguyen, V.H.; Thakur, S.; Raizada, P. CO₂ Photoreduction into Solar Fuels via Vacancy Engineered Bismuth-Based Photocatalysts: Selectivity and Mechanistic Insights. *Chem. Eng. J.* **2022**, *439*, 135563. [[CrossRef](#)]
18. Zhang, Z.; Wang, Y.; Cui, G.; Liu, H.; Abanades, S.; Lu, H. Improvement of CO₂ Photoreduction Efficiency by Process Intensification. *Catalysts* **2021**, *11*, 912. [[CrossRef](#)]
19. Ali, S.; Flores, M.C.; Razzaq, A.; Sorcar, S.; Hiragond, C.B.; Kim, H.R.; Park, Y.H.; Hwang, Y.; Kim, H.S.; Kim, H.; et al. Gas Phase Photocatalytic CO₂ Reduction, "a Brief Overview for Benchmarking". *Catalysts* **2019**, *9*, 727. [[CrossRef](#)]
20. Vega-Mendoza, M.S.; Luévano-Hipólito, E.; Torres-Martínez, L.M. Design and Fabrication of Photocatalytic Coatings with α/β -Bi₂O₃ and Recycled-Fly Ash for Environmental Remediation and Solar Fuel Generation. *Ceram. Int.* **2021**, *47*, 26907–26918. [[CrossRef](#)]
21. Liu, Y.; Ji, G.; Dastageer, M.A.; Zhu, L.; Wang, J.; Zhang, B.; Chang, X.; Gondal, M.A. Highly-Active Direct Z-Scheme Si/TiO₂ Photocatalyst for Boosted CO₂ Reduction into Value-Added Methanol. *RSC Adv.* **2014**, *4*, 56961–56969. [[CrossRef](#)]
22. Low, J.; Cheng, B.; Yu, J. Surface Modification and Enhanced Photocatalytic CO₂ Reduction Performance of TiO₂: A Review. *Appl. Surf. Sci.* **2017**, *392*, 658–686. [[CrossRef](#)]
23. Tang, T.; Yin, Z.; Chen, J.; Zhang, S.; Sheng, W.; Wei, W.; Xiao, Y.; Shi, Q.; Cao, S. Novel P-n Heterojunction Bi₂O₃/Ti₃₊-TiO₂ Photocatalyst Enables the Complete Removal of Tetracyclines under Visible Light. *Chem. Eng. J.* **2021**, *417*, 128058. [[CrossRef](#)]
24. Zhang, X.; Kim, D.; Yan, J.; Lee, L.Y.S. Photocatalytic CO₂ Reduction Enabled by Interfacial S-Scheme Heterojunction between Ultrasmall Copper Phosphosulfide and g-C₃N₄. *ACS Appl. Mater. Interfaces* **2021**, *13*, 9762–9770. [[CrossRef](#)] [[PubMed](#)]
25. Mohamed, R.M.; Harraz, F.A.; Mkhallid, I.A. Hydrothermal Synthesis of Size-Controllable Yttrium Orthovanadate (YVO₄) Nanoparticles and Its Application in Photocatalytic Degradation of Direct Blue Dye. *J. Alloys Compd.* **2012**, *532*, 55–60. [[CrossRef](#)]
26. Mohamed, R.M.; Mkhallid, I.A. Visible Light Photocatalytic Degradation of Cyanide Using Au-TiO₂/Multi-Walled Carbon Nanotube Nanocomposites. *J. Ind. Eng. Chem.* **2015**, *22*, 390–395. [[CrossRef](#)]
27. Ismail, A.A.; Ibrahim, I.A.; Mohamed, R.M. Sol-Gel Synthesis of Vanadia-Silica for Photocatalytic Degradation of Cyanide. *Appl. Catal. B Environ.* **2003**, *45*, 161–166. [[CrossRef](#)]
28. Wang, Z.; Cheng, B.; Zhang, L.; Yu, J.; Tan, H. BiOBr/NiO S-Scheme Heterojunction Photocatalyst for CO₂ Photoreduction. *Sol. RRL* **2022**, *6*, 2100587. [[CrossRef](#)]
29. Mokhtar, M.; Shawky, A. Enhanced Visible-Light-Driven H₂ Evolution over Sol-Gel Prepared Nd₂O₃ Supported with PtO Nanoparticles. *Ceram. Int.* **2022**, *48*, 36670–36677. [[CrossRef](#)]
30. Sharma, A.; Hosseini-bandegharai, A.; Kumar, N.; Kumar, S. Insight into ZnO/Carbon Hybrid Materials for Photocatalytic Reduction of CO₂: An in-Depth Review. *J. CO₂ Util.* **2022**, *65*, 102205. [[CrossRef](#)]
31. Bathla, A.; Lee, J.; Younis, S.A.; Kim, K.H. Recent Advances in Photocatalytic Reduction of CO₂ by TiO₂- and MOF-Based Nanocomposites Impregnated with Metal Nanoparticles. *Mater. Today Chem.* **2022**, *24*, 100870. [[CrossRef](#)]
32. Kadi, M.W.; Mohamed, R.M. Promoted Photocatalytic Hydrogen Evolution over Core-Shellstructured CO₃O₄/TiO₂ under Visible Light. *Int. J. Mater. Technol. Innov.* **2021**, *1*, 1–13.
33. Allam, N.; El-Shazly, A.; Hegazy, A.; Hamza, M.; El Shenawy, E. The Synergetic Effect of Cobalt Content on Enhancing the Photoelectrochemical Hydrogen Production Performance of In-Situ-Doped TiO₂ Photocatalysts. *Int. J. Mater. Technol. Innov.* **2022**, *2*, 20–28. [[CrossRef](#)]

34. Jiang, Z.; Cheng, B.; Zhang, Y.; Wageh, S.; Al-Ghamdi, A.A.; Yu, J.; Wang, L. S-Scheme ZnO/WO₃ Heterojunction Photocatalyst for Efficient H₂O₂ Production. *J. Mater. Sci. Technol.* **2022**, *124*, 193–201. [[CrossRef](#)]
35. Li, J.; Zhang, M.; Guan, Z.; Li, Q.; He, C.; Yang, J. Synergistic Effect of Surface and Bulk Single-Electron-Trapped Oxygen Vacancy of TiO₂ in the Photocatalytic Reduction of CO₂. *Appl. Catal. B Environ.* **2017**, *206*, 300–307. [[CrossRef](#)]
36. Zou, Z.; Xie, C.; Zhang, S.; Yu, X.; Zou, T.; Li, J. Preparation and Photocatalytic Activity of TiO₂/CeO₂/Bi₂O₃ Composite for Rhodamine B Degradation under Visible Light Irradiation. *J. Alloys Compd.* **2013**, *581*, 385–391. [[CrossRef](#)]
37. Hezam, A.; Namratha, K.; Drmosh, Q.A.; Yamani, Z.H.; Byrappa, K. Synthesis of Heterostructured Bi₂O₃–CeO₂–ZnO Photocatalyst with Enhanced Sunlight Photocatalytic Activity. *Ceram. Int.* **2017**, *43*, 5292–5301. [[CrossRef](#)]
38. Sabzehmeidani, M.M.; Karimi, H.; Ghaedi, M. Nanofibers Based Quaternary CeO₂/CO₃O₄/Ag/Ag₃PO₄ S-Scheme Heterojunction Photocatalyst with Enhanced Degradation of Organic Dyes. *Mater. Res. Bull.* **2022**, *147*, 111629. [[CrossRef](#)]
39. Zhao, Y.; Lin, C.; Zhang, L.; Meng, X.; Tang, H. Bi₂O₃ Induced Tremella-like Bi₂WO₆ with Visible Light Catalytic Performance. *Ceram. Int.* **2022**, *48*, 4584–4594. [[CrossRef](#)]
40. He, W.; Wei, Y.; Xiong, J.; Tang, Z.; Wang, Y.; Wang, X.; Deng, J.; Yu, X.; Zhang, X.; Zhao, Z. Boosting Selective Photocatalytic CO₂ Reduction to CO over Dual-Core@shell Structured Bi₂O₃/Bi₂WO₆@g-C₃N₄ Catalysts with Strong Interaction Interface. *Sep. Purif. Technol.* **2022**, *300*, 121850. [[CrossRef](#)]
41. Hezam, A.; Namratha, K.; Drmosh, Q.A.; Ponnamm, D.; Wang, J.; Prasad, S.; Ahamed, M.; Cheng, C.; Byrappa, K. CeO₂ Nanostructures Enriched with Oxygen Vacancies for Photocatalytic CO₂ Reduction. *ACS Appl. Nano Mater.* **2020**, *3*, 138–148. [[CrossRef](#)]
42. Xu, L.; Zeng, J.; Li, Q.; Luo, X.; Chen, T.; Liu, J.; Wang, L.L. Multifunctional Silicene/CeO₂ Heterojunctions: Desirable Electronic Material and Promising Water-Splitting Photocatalyst. *Chin. Chem. Lett.* **2022**, *33*, 3947–3950. [[CrossRef](#)]
43. Cui, Z.; Zhang, D.; Hu, J.; Fang, C. CdS/CeO₂ Heterostructures as Visible-Light Photocatalysts for the Reduction of Nitro to Amine Organics. *J. Alloys Compd.* **2021**, *885*, 160961. [[CrossRef](#)]
44. Wu, D.; Zhang, X.; Liu, S.; Ren, Z.; Xing, Y.; Jin, X.; Ni, G. Fabrication of a Z-Scheme CeO₂/Bi₂O₄ Heterojunction Photocatalyst with Superior Visible-Light Responsive Photocatalytic Performance. *J. Alloys Compd.* **2022**, *909*, 164671. [[CrossRef](#)]
45. Hsieh, S.H.; Manivel, A.; Lee, G.J.; Wu, J.J. Synthesis of Mesoporous Bi₂O₃/CeO₂ Microsphere for Photocatalytic Degradation of Orange II Dye. *Mater. Res. Bull.* **2013**, *48*, 4174–4180. [[CrossRef](#)]
46. Cui, S.; Ma, Q.; Chen, H.; Zhang, Y.; Sun, F. Heterojunction G-C₃N₄/CeO₂/Bi₂O₃ Composite for the Photocatalytic Purification of Exhaust Gas. *Mater. Chem. Phys.* **2022**, *285*, 126081. [[CrossRef](#)]
47. Nie, J.; Zhu, G.; Zhang, W.; Gao, J.; Zhong, P.; Xie, X.; Huang, Y.; Hojamberdiev, M. Oxygen Vacancy Defects-Boosted Deep Oxidation of NO by β-Bi₂O₃/CeO₂-δ p-n Heterojunction Photocatalyst in Situ Synthesized from Bi/Ce(CO₃)(OH) Precursor. *Chem. Eng. J.* **2021**, *424*, 130327. [[CrossRef](#)]
48. Yang, X.; Zhang, Y.; Wang, Y.; Xin, C.; Zhang, P.; Liu, D.; Mamba, B.B.; Kefeni, K.K.; Kuvarega, A.T.; Gui, J. Hollow β-Bi₂O₃@CeO₂ Heterostructure Microsphere with Controllable Crystal Phase for Efficient Photocatalysis. *Chem. Eng. J.* **2020**, *387*, 124100. [[CrossRef](#)]
49. Masula, K.; Bhongiri, Y.; Raghav Rao, G.; Vijay Kumar, P.; Pola, S.; Basude, M. Evolution of Photocatalytic Activity of CeO₂–Bi₂O₃ Composite Material for Wastewater Degradation under Visible-Light Irradiation. *Opt. Mater.* **2022**, *126*, 112201. [[CrossRef](#)]
50. Li, X.; Guan, J.; Jiang, H.; Song, X.; Huo, P.; Wang, H. RGO Modified R-CeO₂/g-C₃N₄ Multi-Interface Contact S-Scheme Photocatalyst for Efficient CO₂ Photoreduction. *Appl. Surf. Sci.* **2021**, *563*, 150042. [[CrossRef](#)]
51. Li, L.; Yan, B. CeO₂-Bi₂O₃ Nanocomposite: Two Step Synthesis, Microstructure and Photocatalytic Activity. *J. Non Cryst. Solids* **2009**, *355*, 776–779. [[CrossRef](#)]
52. Albukhari, S.M.; Shawky, A. Ag/Ag₂O-Decorated Sol-Gel-Processed TeO₂ Nanojunctions for Enhanced H₂ Production under Visible Light. *J. Mol. Liq.* **2021**, *336*, 116870. [[CrossRef](#)]
53. Prajapati, P.K.; Malik, A.; Nandal, N.; Pandita, S.; Singh, R.; Bhandari, S.; Saran, S.; Jain, S.L. Morphology Controlled Fe and Ni-Doped CeO₂ Nanorods as an Excellent Heterojunction Photocatalyst for CO₂ Reduction. *Appl. Surf. Sci.* **2022**, *588*, 152912. [[CrossRef](#)]
54. Kadi, M.W.; Mohamed, R.M.; Ismail, A.A.; Bahnemann, D.W. Soft and Hard Templates Assisted Synthesis Mesoporous CuO/g-C₃N₄ Heterostructures for Highly Enhanced and Accelerated Hg(II) Photoreduction under Visible Light. *J. Colloid Interface Sci.* **2020**, *580*, 223–233. [[CrossRef](#)]
55. Kadi, M.W.; Mohamed, R.M.; Ismail, A.A.; Bahnemann, D.W. Performance of Mesoporous α-Fe₂O₃/g-C₃N₄ Heterojunction for Photoreduction of Hg(II) under Visible Light Illumination. *Ceram. Int.* **2020**, *46*, 23098–23106. [[CrossRef](#)]
56. Kadi, M.W.; Mohamed, R.M.; Ismail, A.A.; Bahnemann, D.W. Decoration of G-C₃N₄ Nanosheets by Mesoporous CoFe₂O₄ Nanoparticles for Promoting Visible-Light Photocatalytic Hg(II) Reduction. *Colloids Surf. A Physicochem. Eng. Asp.* **2020**, *603*, 125206. [[CrossRef](#)]
57. Shawky, A.; Alhaddad, M.; Al-Namshah, K.S.; Mohamed, R.M.; Awwad, N.S. Synthesis of Pt-Decorated CaTiO₃ Nanocrystals for Efficient Photoconversion of Nitrobenzene to Aniline under Visible Light. *J. Mol. Liq.* **2020**, *304*, 112704. [[CrossRef](#)]
58. Mohamed, R.M.; Shawky, A. CNT Supported Mn-Doped ZnO Nanoparticles: Simple Synthesis and Improved Photocatalytic Activity for Degradation of Malachite Green Dye under Visible Light. *Appl. Nanosci.* **2018**, *8*, 1179–1188. [[CrossRef](#)]
59. Mohamed, R.M.; McKinney, D.; Kadi, M.W.; Mkhaliid, I.A.; Sigmund, W. Platinum/Zinc Oxide Nanoparticles: Enhanced Photocatalysts Degrade Malachite Green Dye under Visible Light Conditions. *Ceram. Int.* **2016**, *42*, 9375–9381. [[CrossRef](#)]

60. Kadi, M.W.; McKinney, D.; Mohamed, R.M.; Mkhaliid, I.A.; Sigmund, W. Fluorine Doped Zinc Oxide Nanowires: Enhanced Photocatalysts Degrade Malachite Green Dye under Visible Light Conditions. *Ceram. Int.* **2016**, *42*, 4672–4678. [[CrossRef](#)]
61. Rajendran, S.; Khan, M.M.; Gracia, F.; Qin, J.; Gupta, V.K.; Arumainathan, S. Ce₃₊-Ion-Induced Visible-Light Photocatalytic Degradation and Electrochemical Activity of ZnO/CeO₂ Nanocomposite. *Sci. Rep.* **2016**, *6*, 1–11. [[CrossRef](#)] [[PubMed](#)]
62. Channei, D.; Chansaenpak, K.; Phanichphant, S.; Jannoey, P.; Khanitchaidecha, W.; Nakaruk, A. Synthesis and Characterization of WO₃/CeO₂ Heterostructured Nanoparticles for Photodegradation of Indigo Carmine Dye. *ACS Omega* **2021**, *6*, 19771–19777. [[CrossRef](#)] [[PubMed](#)]
63. Basaleh, A.S.; Shawky, A.; Zaki, Z.I. Visible Light-Driven Photodegradation of Ciprofloxacin over Sol-Gel Prepared Bi₂O₃-Modified La-Doped NaTaO₃ Nanostructures. *Ceram. Int.* **2021**, *47*, 19205–19212. [[CrossRef](#)]
64. Shawky, A.; Mohamed, R.M. S-Scheme Heterojunctions: Emerging Designed Photocatalysts toward Green Energy and Environmental Remediation Redox Reactions. *J. Environ. Chem. Eng.* **2022**, *10*, 108249. [[CrossRef](#)]
65. Zhang, L.; Zhang, J.; Yu, H.; Yu, J. Emerging S-Scheme Photocatalyst. *Adv. Mater.* **2022**, *34*, 2107668. [[CrossRef](#)]
66. Xu, Q.; Zhang, L.; Cheng, B.; Fan, J.; Yu, J. S-Scheme Heterojunction Photocatalyst. *Chem* **2020**, *6*, 1543–1559. [[CrossRef](#)]
67. Shawky, A.; Mohamed, R.M.; Alahmadi, N.; Zaki, Z.I. Enhanced Photocatalytic Reduction of Hexavalent Chromium Ions over S-Scheme Based 2D MoS₂-Supported TiO₂ Heterojunctions under Visible Light. *Colloids Surf. A Physicochem. Eng. Asp.* **2022**, *641*, 128564. [[CrossRef](#)]
68. Alhaddad, M.; Shawky, A. Pt-Decorated ZnMn₂O₄ Nanorods for Effective Photocatalytic Reduction of CO₂ into Methanol under Visible Light. *Ceram. Int.* **2021**, *47*, 9763–9770. [[CrossRef](#)]
69. Lais, A.; Gondal, M.A.; Dastageer, M.A. Semiconducting Oxide Photocatalysts for Reduction of CO₂ to Methanol. *Environ. Chem. Lett.* **2018**, *16*, 183–210. [[CrossRef](#)]
70. Pocovi-Martínez, S.; Zumeta-Dube, I.; Diaz, D. Production of Methanol from Aqueous CO₂ by Using Co₃O₄ Nanostructures as Photocatalysts. *J. Nanomater.* **2019**, *2019*, 1–10. [[CrossRef](#)]
71. Pal, N.; Lee, J.H.; Cho, E.B. Recent Trends in Morphology-Controlled Synthesis and Application of Mesoporous Silica Nanoparticles. *Nanomaterials* **2020**, *10*, 2122. [[CrossRef](#)] [[PubMed](#)]